Fabry-Pérot resonant avalanche-mode silicon LEDs for tunable narrow-band emission

Dutta, S.; Verbiest, G.J.

DOI
10.1364/OE.471368

Publication date
2022

Document Version
Final published version

Published in
Optics Express

Citation (APA)
Dutta, S., & Verbiest, G. J. (2022). Fabry-Pérot resonant avalanche-mode silicon LEDs for tunable narrow-band emission. *Optics Express*, *30*(23), 42323-42335. https://doi.org/10.1364/OE.471368

Research Article Vol. 30, No. 23 / 7 Nov 2022 / *Optics Express* 42323

Optics EXPRESS

Fabry-Pérot resonant avalanche-mode silicon LEDs for tunable narrow-band emission

SATADAL DUTTA[*] **AND GERARD J. VERBIEST**

Precision and Microsystems Engineering, Delft University of Technology, Mekelweg 2, 2628CD, Delft, The Netherlands
[*]*s.dutta-1@tudelft.nl*

Abstract: We report on the effect of Fabry-Pérot (FP) resonance on hot-carrier electroluminescence (EL) spectra and the optical power efficiencies of silicon (Si) avalanche-mode (AM) LEDs in the wavelength range from 500 nm to 950 nm. The LEDs, fabricated in a silicon-on-insulator photonics technology, consist of symmetric p-n junctions placed within a 0.21 μm thick Si micro-ring of varying width and radius. We show that the peak wavelength in the EL-spectra can be tuned within a range of 100 nm by varying the ring width from 0.16 μm to 0.30 μm, which is explained by FP resonance. The measured EL-spectra features relatively narrow bands (with a spectral width of ~50 nm) with high intensities compared to conventional Si AMLEDs. By varying the ring radius and using a high doping level, we obtain a record high optical power efficiency of 3.2×10^{-5}. Our work is a breakthrough in engineering the EL spectrum of Si, foreseen to benefit the performance of Si-integrated optical interconnects and sensors.

1. Introduction

Silicon (Si) photonics [1] plays a central role in the monolithic integration of passive optical components and photodetectors for applications in biochemical sensing [2,3], data communication [4,5], and imaging [6]. At the same time, Si has not been suitable for developing efficient light sources, due to its indirect bandgap. This results in low quantum efficiencies for electroluminescence (EL) in Si p-n junctions [7–9]. Driven by the success of Si Complementary Metal-Oxide-Semiconductor (CMOS) technology and a growing demand for on-chip functionality, research on viable Si light-sources has recently gained momentum [10–15]. In particular, the avalanche-mode (AM) EL spectrum of Si [8,16–18] spans a wavelength (λ) range of 450 nm$<\lambda<$ 950 nm, which has a significant overlap with the spectral responsivity of Si photodiodes [12,19], with the range of human vision [20], and with the absorption spectrum of various biochemical entities [21,22]. As such, despite the low optical power efficiency ($\eta_{\text{opt}} \sim 10^{-6}$), Si avalanche-mode light-emitting diodes (AMLEDs) have been emerging as viable light-sources in applications where high intensity and coherence are not mandatory, e.g. monolithic optical links [10,13,23], pigment sensors [24], and CMOS micro-displays [25]. To boost the performance of such systems, desired features for future Si AMLEDs are an increased η_{opt}, as well as a control over the peak wavelength λ_{p}, and a reduction in its corresponding full-width half maximum (FWHM), without altering material composition or fabrication process. Realizing these features is beneficial for decreasing energy consumption per bit in monolithic optical links [13,26], or for increasing sensor resolution and specificity [27–29].

The mechanism of light emission in AMLEDs is phonon assisted recombination between hot electrons and holes [30], which are accelerated to energies as high as 2.5 eV by the electric field in the p-n junction. Several efforts have been made till date to achieve the aforesaid AMLED features using commercial Si-CMOS and Si-bipolar technologies. These include carrier injection in a 3-terminal device [8], carrier energy and momentum engineering [30,31], superjunction LEDs [32], and gated Field-effect transistor (FET)-based LEDs [25,33,34]. These techniques, which include the authors' previous works, target only the electronic properties of

#471368 https://doi.org/10.1364/OE.471368
Journal © 2022 Received 28 Jul 2022; revised 16 Sep 2022; accepted 21 Sep 2022; published 2 Nov 2022

the light-emitting junction, where AMLED designs were explored based on varying doping and electric-field profiles in standard CMOS technologies. However, spontaneous emission of light is also dependent on the optical mode density [35]. Yet, there is still the question how optical cavity resonances within the Si LED can impact its phonon-assisted AM EL-spectrum. Till date, cavity resonances were used for engineering the spectral line-widths of nanocrystal LEDs [36], organic LEDs [37], Er-doped Si-SiO_2 infrared LEDs [38], III-V light-sources [39,40], for enhancing infrared responsivity of Si photodiodes [41,42], and responsivity of photodiodes based on 2D materials [43]. Cavity based nanostructures are also used in spatial manipulation of nanoacoustic waves [44], when excited by laser pulses. In this work, we explore the effects of optical cavity resonances on the EL-spectra and η_{opt} of Si AMLEDs using a recently developed CMOS-compatible Si-photonics technology. We show the effect of Fabry-Pérot (FP) resonance [45,46] resulting from the LED geometry on its λ_{p} and thus, its color.

The paper is organized as follows. Section 2 describes the design of the LEDs and section 3 describes the experimental method used to characterize the opto-electronic behavior of the LEDs. In sections 4.1–4.3, we present the measurement results of the electrical *I*-*V* characteristics, the EL spectra and the optical power efficiency of the LEDs, respectively. Section 5 discusses the main results, potential applications, and future recommendations based on this work. Finally, section 6 concludes this work.

2. Design of micro-ring AMLEDs

The AMLED consists of a Si micro-ring of radius R and width w, with symmetrically-doped half-rings forming a p-n junction parallel to the y-axis as shown in Figs. 1(a) and (b). Straight p- and n-doped Si strips branch off the ring periphery along the x-axis terminating in 5 μm x 5 μm Si blocks. Highly doped p^+ and n^+ implants are placed on top of these blocks to form electrical contacts to bond pads for biasing. Multiple rings (a total of eleven) are placed in an array with a pitch of 5 μm, and connected in parallel to increase the total junction (and thereby the light-emission) area. Figure 1(b) shows the AMLED cross-section, along the x-axis (cut-line), in a 130 nm Si-on-insulator (SOI) photonics technology (iSiPP50G) [47] from IMEC. The SOI layer thickness post-fabrication of device is 0.21 μm. This technology offers both active and passive photonic components, aimed primarily at NIR telecommunication applications.

A total of 21 LEDs were fabricated with design variations, with each having a unique R, w, and doping level. Two doping levels were used, namely N1-P1 (sheet resistances of R_{N}=2005 Ω/sq. and R_{P}=6672 Ω/sq. respectively) and N2-P2 (sheet resistances of R_{N}=638 Ω/sq. and R_{P}=1020 Ω/sq. respectively). For both doping levels, LEDs were fabricated with R varying from 0.6 μm to 2.0 μm and a constant $w = 0.3$ μm. We used a minimum ring radius (R) of 0.6 μm to avoid critical design errors, and increased it in steps of 0.1 μm. In addition, for the higher doping level N2-P2, LEDs with w varying from 0.16 μm to 0.30 μm were designed, keeping a constant $R = 2.0$ μm. The technology has a minimum allowed w of 0.15 μm, with a fabrication accuracy of 15 nm. Therefore, we used 0.16 μm as the smallest w, and increased it in steps of 20 nm. Post-fabrication, a 15 nm broadening in the width is specified by the foundry relative to the designed value of w. Figure 1(c) shows the top-view micrograph of the LED with $R = 2.0$ μm and $w = 0.3$ μm, captured with a Keyence VHX optical microscope.

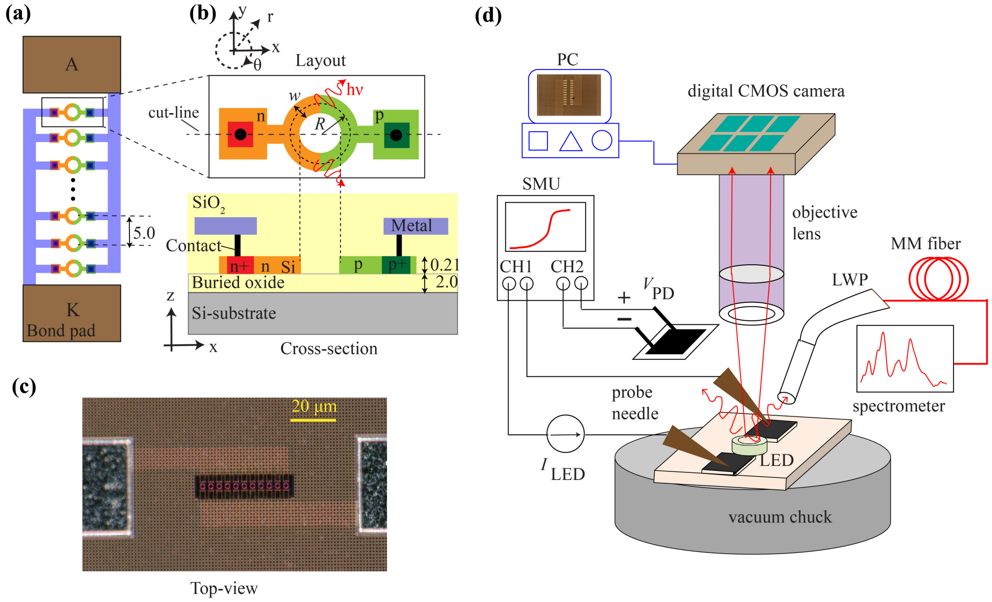

Fig. 1. (a) Schematic layout of a micro-ring avalanche-mode light-emitting diode (AMLED), and (b) a zoom-in on a single micro-ring unit along with its device cross-section (along the indicated dashed cut-line) in iSiPP50G silicon photonics technology [47]. Labels x, y, z denote Cartesian coordinate axes while r (radial) and θ (azimuthal) denote polar coordinate axes. The doping levels (n and p), ring width w and radius R are varied in the LED designs. Indicated dimensions are in μm. (c) Top-view optical micrograph of the fabricated LED with w=0.3 μm and R=2.0 μm. (d) Schematic of the opto-electronic measurement set-up (illustrations are not to scale). The LED bond pads are electrically biased via a precision SMU. The fiber pigtail of a lightwave probe (LWP) couples the emitted light to the spectrometer via a multi-mode (MM) optical fiber. The digital CMOS camera records the AM-EL micrographs of the LED. The reverse biased Si PD is used to measure the emitted optical power in air.

3. Experimental method

Figure 1(d) shows the schematic LED characterization set-up. The reverse biased electrical I_{LED}-V_{LED} characteristics were measured in a probe-station. The LED bond pads (anode and cathode) were biased via a Keysight B2912A precision source and measurement unit (SMU). For optical characterization, the LEDs were reverse-biased in constant current mode (I_{LED}). The AM EL-spectra were measured in the range 500 nm$<\lambda<$ 950 nm by mounting a multi-mode fiber pigtail of a lightwave probe (LWP) from Form Factor Inc. on top of the die. The LWP has a negligible ($<$ 0.5 dB insertion loss) in our spectral range of interest. The LWP was then fed to an AvaSpec ULS2048CL-EVO spectrometer via a multi-mode optical fiber. We recorded the spectra with a 20 s integration time (T_{int}). The spectral irradiance $\varepsilon(\lambda)$ was obtained by normalizing the intensities w.r.t. the integrated intensity (i.e. $\int \varepsilon(\lambda) \cdot \mathrm{d}\lambda = 1$).

The AM EL micrograph of the LEDs was captured with an integration time of 20 s via a CS165MU digital camera mounted on top of the microscope objective. The optical power P_{opt}, emerging out of the chip, was measured via a BPW34 Si photodiode (PD) mounted on top of the LED (Fig. 1(d)) and reverse biased by the SMU. The dark current of the photodiode was first subtracted from the measured PD current to obtain the photocurrent I_{PD}). The PD subtends a solid angle of $\approx \pi$ sr at the chip surface. The photocurrents obtained by detecting the light from the individual the LEDs ($I_{\text{PD}}(R, w)$) were converted to corresponding P_{opt} via a two-step calibration. Firstly, the optical power P_{cal} of a reference fiber-coupled light source (AvaLight DH-S-BAL) at λ = 800 nm was measured with a ThorLabs S155C photoreceiver and PM100D power meter. The same P_{cal} was measured in terms of the spectrometer counts per second (C_{cal}). Secondly, as the photocurrent varies linearly with the light-intensity, the resulting P_{opt} was calculated as:

$$P_{\text{opt}}(R,w)=\frac{I_{\text{PD}}(R,w)[\text{A}]}{I_{\text{PD}}(\text{ref})[\text{A}]}\times\frac{P_{\text{cal}}[\mu\text{W}]}{C_{\text{cal}}[\text{counts/s}]}\times\frac{\int E_{\text{ref}}(\lambda)\cdot \text{d}\lambda[\text{counts}]}{T_{\text{int}}[\text{s}]},\tag{1}$$

where $I_{\text{PD}}(\text{ref})$ is the PD photocurrent of the LED with w = 0.3 μm, and R = 2.0 μm. $E_{\text{ref}}(\lambda)$ is the spectral count of this reference LED measured by the spectrometer. Subsequently, the $\eta_{\text{opt}}(R, w)$ was calculated as the ratio of optical to electrical power of the LED: $P_{\text{opt}}(R, w)/(V_{\text{LED}} \cdot I_{\text{LED}})$.

4. Results

The results are organized as follows. Section 4.1 describes the measured electrical I-V characteristics and breakdown voltages of the micro-ring LEDs. Section 4.2 describes the EL properties of these LEDs, and the dependency of the spectral irradiance on the LED geometry. Calculated Fabry-Pérot resonances are also described to explain the experimental trends. Section 4.3 describes the measured optical power efficiency of the micro-ring LEDs and benchmarks the LED performance against prior art.

4.1. AMLED electrical I-V characteristics

Figure 2(a) shows the measured avalanche-mode current-voltage (I_{LED}-V_{LED}) characteristics of the LEDs with R = 2.0 μm for the two doping levels. The avalanche breakdown voltage (V_{BR}) is defined for all LEDs at a fixed current of I_{LED} = 100 μA. The N1-P1 LEDs have a V_{BR} near 14 V, while the N2-P2 LEDs have a V_{BR} near 7 V. This is because N2-P2 doping level is higher than N1-P1, and hence the critical electric field at the p-n junction is attained at a smaller V_{LED} [48]. Further, we observe that V_{BR} shows a weak linear dependence on R/w as shown in Fig. 2(b), spanning a range of $\Delta V_{\text{BR}} \approx 1$ V. This range is greater than the observed variation in V_{BR} (± 0.15 V) for a single LED across multiple dies on the wafer (see Fig. 2(c)). The V_{BR} dependence can be partly attributed to the contribution of series resistance ($\propto \pi \cdot R/w$) of the doped rings to V_{LED}, considering high current densities ($\sim 10^4$ A·cm^{-2}) through the narrow p-n junctions.

4.2. AMLED electroluminescence and spectral irradiance

Figure 2(d) shows the top-view optical micrograph of the fabricated N2-P2 doped LED with w=0.3 μm and R=2.0 μm, and Fig. 2(e) shows the AM EL micrograph captured at I_{LED} = 2 mA. Localized light emission, in the form of bright twin spots, is observed from the two p-n junctions of each ring (see zoom-in insets). This is expected as AM EL stems from recombination of hot carriers (electrons/holes) generated by the high electric field within the space-charge region [30,49]. However, the intensity of the spots attenuates sharply along the θ-axis of the ring, which is due to the high absorption of light at short λ by Si.

Figure 3(a) shows the mean and standard deviation in the $\varepsilon(\lambda)$ of the N2-P2 doped LED with R=2.0 μm, w = 0.3 μm, when measured in multiple dies on the wafer. Across dies, small variations in the intensity are observed and no significant variation in the spectral shape are observed. Figure 3(b) shows the $\varepsilon(\lambda)$ of the LEDs with doping levels N1-P1 and N2-P2, both of the same geometry (R=2.0 μm, w = 0.3 μm). In both the LEDs, two dominant bands are observed: VIS band peaking at $\lambda_{\text{VIS}} \approx 620$ nm with a full-width at half-maximum (FWHM) of 53 nm, and an NIR band peaking at $\lambda_{\text{NIR}} \approx 765$ nm with a FWHM of 66 nm. Additionally, two minor bands near 550 nm and 700 nm are observed. No significant difference in the $\varepsilon(\lambda)$ between the two LEDs are observed, when compared to the variations in $\varepsilon(\lambda)$ for a single LED across

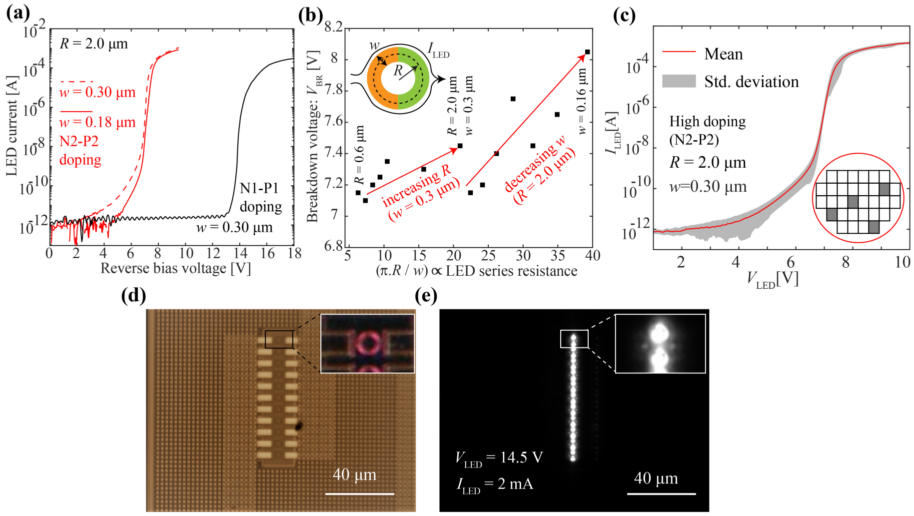

Fig. 2. (a) AM I-V characteristics of the LEDs with the indicated dimensions. The doping level N2-P2 is higher than N1-P1. Breakdown voltage $V_{\mathrm{BR}} \sim 14$ V for the N1-P1 LEDs and ~ 7 V for the N2-P2 LEDs, defined for each LED at I_{LED}=100 μA. (b) Dependence of the measured V_{BR} on R and w. The inset depicts current flow pathway along the two parallel pathways formed by the semi-rings. (c) Mean and std. deviation of the AM I-V characteristics of the LED (w=0.3 μm and R=2.0 μm) across multiple dies with locations on the wafer (marked in grey blocks) in the inset. (d) Top-view of the LED along with (e) its AM-EL micrograph captured for an integration time of 20 s at the indicated bias.

multiple dies on the wafer. For comparison, a typical wide-band $\varepsilon(\lambda)$ of a conventional n$^+$p AMLED [32] with a $V_{\mathrm{BR}} \approx 17$ V is also shown in Fig. 3(b), which was fabricated in a CMOS technology with a thicker SOI layer (≈ 1.5 μm) and with no lateral optical confinement.

The intensities of the VIS and NIR bands are observed to be ~ 2 times higher than that of the two neighbouring minor bands near 550 nm and 700 nm. Such an enhancement of intensity and of the quality factor (λ_{VIS} / FWHM ≈ 12) is ~ 2 times higher than that in prior reported Si AMLEDs [32,50]. Next, we observe that varying R has a negligible effect on $\varepsilon(\lambda)$, as shown in Fig. 3(c),(d). This indicates a lack of any resonance of guided modes along the θ-axis of the ring; the high optical absorption coefficient of Si [51] significantly reduces the lifetime of a photon at short wavelengths traversing around the ring. As a quantitative estimate, the attenuation length in Si ranges between 1–10 μm for λ in the range 500–700 nm, which are close to the round-trip length of the micro-rings (4–12 μm). This is also supported by the spot-like light-emission profile observed in the AM-EL micrographs in Fig. 2(e). Note that for guided TE and TM modes to be excited along θ-axis, the estimated radiation loss coefficients [52,53] are $\sim 5 \times 10^{-7}$ and $\sim 7 \times 10^{-6}$ respectively, for $R = 0.6$ μm, and $w = 0.3$ μm, which are much smaller than the extinction coefficient of Si ($\sim$0.01) at $\lambda \sim 700$ nm. Hence, material absorption is the dominant factor in the observed light-emission profile.

The LEDs are optically confined along the r-axis by the ring width w and along the z-axis by t_{Si}. Both w and t_{Si} have the same order of magnitude as λ/n_{Si} where n_{Si} is the refractive index of Si [51]. Thus, we hypothesize that the LED spectral behavior is attributed to Fabry-Pérot (FP) resonances both along the width (r-axis) and thickness (z-axis). Note that the conventional n$^+$p AMLED (EL-spectrum shown in grey in Fig. 3(b)) was fabricated in a different SOI technology [54] comprising a uniform 1.5 μm thick SOI layer without any lateral confinement. As such, no optical resonances could be observed in the measured wavelength range.

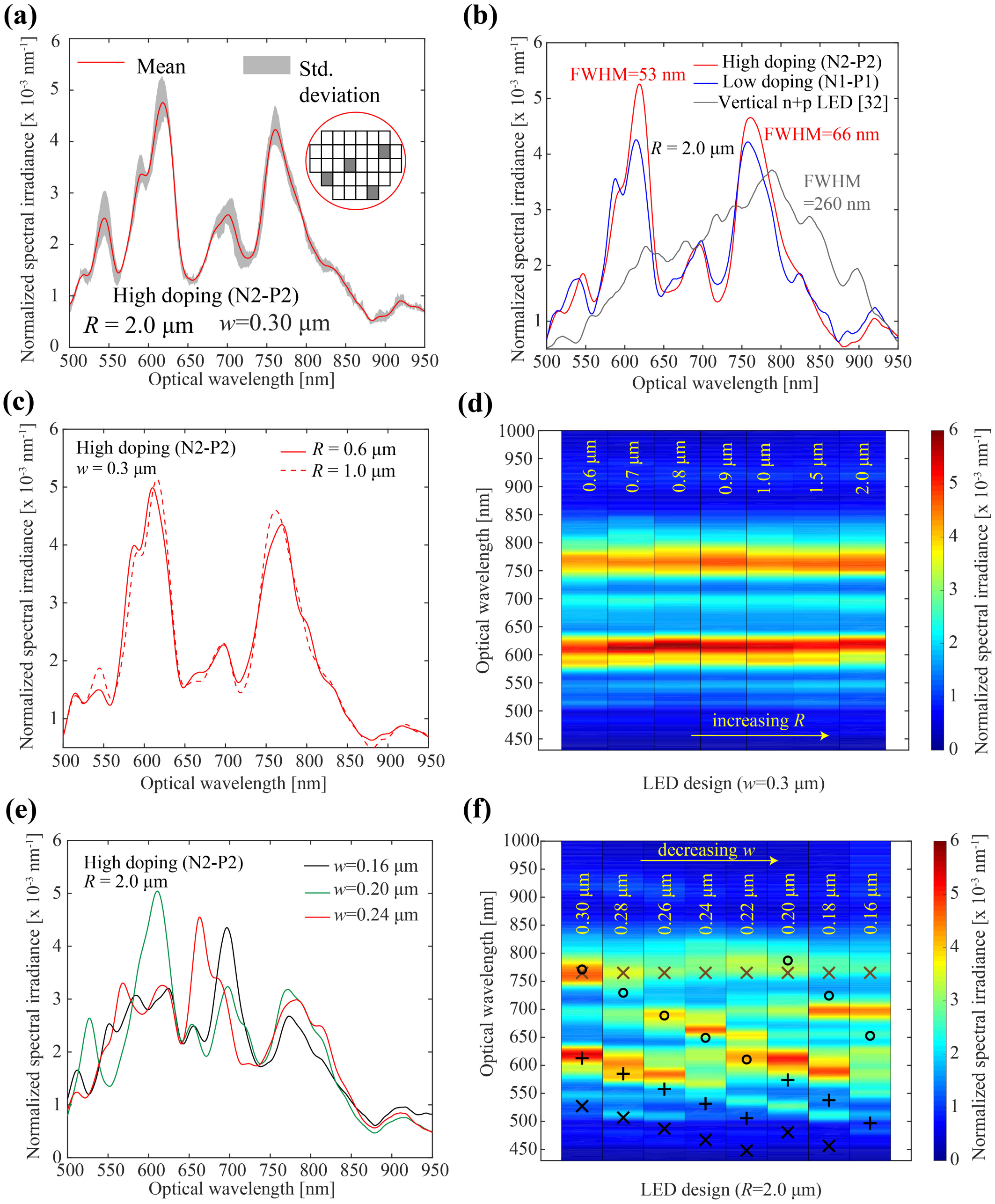

Fig. 3. (a) Measured AM spectral irradiance of the same LED showing the mean and std. deviation across multiple dies on the wafer with locations shown in the inset. Comparison between the normalized $\varepsilon(\lambda)$ of the LEDs with (b) varying doping levels (also shown in grey is the $\varepsilon(\lambda)$ for a prior reported n^+p AMLED [32]), (c) varying R, and (e) varying w. Panels (d) and (f) show the corresponding color plots of $\varepsilon(\lambda)$ as a function of R, and w respectively. The black symbols **o**,**+**,**x** in panel (f) represent the calculated Fabry-Pérot resonance peaks (λ_m, m=2,3, and 4 respectively) versus w, while the brown symbols represent $\lambda_{m=2}$ at 765 nm due to t_{Si}= 0.21 μm.

To validate our hypothesis on FP resonance in the LEDs, we show the $\varepsilon(\lambda)$ for a fixed R and varying w (see Figs. 3(e),(f)). The NIR band is consistently observed in the spectrum for each w. Moreover, we observe intensity peaks appearing at specific wavelengths λ_P spanning across the visible spectrum (500-750 nm); λ_P exhibits a blue shift as w increases. We explain this behavior via the analytical model for the transmission coefficient $T(\lambda)$ of a FP resonator (etalon) [46]. For a lossy Si cavity with extinction coefficient $k_\mathrm{Si}(\lambda)$ [51], placed between two Si-SiO$_2$ interfaces of Fresnel reflection coefficient $R(\lambda)$ each, we have

$$T_\mathrm{FP}(\lambda) = \frac{[1 - R(\lambda)]^2 \cdot \exp\left(-\alpha_\mathrm{Si} \cdot d\right)}{[1 - R(\lambda) \cdot \exp\left(-\alpha_\mathrm{Si} \cdot d\right)]^2 + 4R(\lambda) \cdot \exp\left(-\alpha_\mathrm{Si} \cdot d\right) \cdot \sin^2 \phi(\lambda)}, \tag{2}$$

where

$$R(\lambda) = \left[\frac{n_\mathrm{Si}(\lambda) - n_\mathrm{ox}(\lambda)}{n_\mathrm{Si}(\lambda) + n_\mathrm{ox}(\lambda)}\right]^2, \tag{3}$$

$$\phi(\lambda) = \frac{2\pi \cdot n_\mathrm{Si}(\lambda) \cdot d}{\lambda}, \tag{4}$$

and

$$\alpha_\mathrm{Si}(\lambda) = \frac{4\pi \cdot k_\mathrm{Si}(\lambda)}{\lambda}. \tag{5}$$

For our LEDs, we calculate two independent $T_\mathrm{FP}(\lambda)$ corresponding to in-plane (r-axis) and out-of-plane (z-axis) FP resonators, where we substitute d=w and d=t_Si in Eq. (2), respectively. Figure 4 shows the calculated $T_\mathrm{FP}(\lambda)$ for both r-axis and z-axis resonances alongside the EL-spectra of the LEDs with varying w. In our calculation, we used $d = (w{+}15)$ nm, to account for the broadening due to fabrication process. $T_\mathrm{FP}(\lambda)$ features local maxima at resonance wavelengths λ_m when $\phi(\lambda_\mathrm{m}) = \mathrm{m}\pi$, where m is the mode order and takes integer values. We observe a good agreement between λ_m and the λ_P in the measured EL-spectra. Figure 3(f) shows an overlay of the calculated λ_m via symbols on top of the color plot of $\varepsilon(\lambda)$. The black symbols correspond to the λ_m for in-plane (r-axis) resonances for m=2, 3, and 4; the brown crosses (see Fig. 3(f)) correspond to the out-of-plane (z-axis) resonance at λ_2 = 765 nm. Note that the fundamental mode $\lambda_\mathrm{m=1}$ occurs near 1600 nm and lies far beyond our spectral range of the LED. Thus, we observe that FP resonance aptly explains the observed trends in λ_P of measured $\varepsilon(\lambda)$.

4.3. Optical power efficiency

Figure 5(a) shows the measured P_opt of the indicated AMLEDs as a function of $P_\mathrm{LED} = I_\mathrm{LED} \cdot V_\mathrm{LED}$, where I_LED is varied from 1 mA to 10 mA in all the LEDs, in steps of 1 mA. We observe that P_opt exhibits a linear dependence on P_LED for the N2-P2 LEDs, but exhibits a sub-linear dependence for the N1-P1 LEDs for the same ring geometry (and hence the same current density). This is likely due to a higher series resistance and consequently self-heating at higher P_LED in the N1-P1 doped LEDs, which can reduce the internal quantum efficiency [55]. Similar observations were reported in AMLEDs in standard SOI technologies [12] and in gated CMOS based AMLEDs [34]. A linear P_opt-P_LED relationship is advantageous for realizing small-signal modulators [34] in switched AMLEDs. In a prior work [12], self-heating effects on SOI optocouplers were analyzed in detail and the linearity was shown to improve via placement of integrated heat sinks. In another work [34], an extended linear regime and a higher slope of P_opt-I_LED curve were shown using three-terminal FET based devices. Figure 5(b) summarizes the optical power efficiency $\eta_\mathrm{opt}(R, w)$ for all the LED designs in this work. We obtain the highest $\eta_\mathrm{opt} \approx 3.2{\times}10^{-5}$ for the N2-P2 LED with $R = 0.6$ μm and $w = 0.3$ μm, which also has the lowest V_BR (≈ 7 V), and the lowest device footprint ($22\pi \cdot R \cdot w \approx 12$ $\mu\mathrm{m}^2$ per LED). Further, η_opt decreases with increasing R and decreasing w, which is consistent with the dependence of V_BR on R and w (Fig. 2(b)).

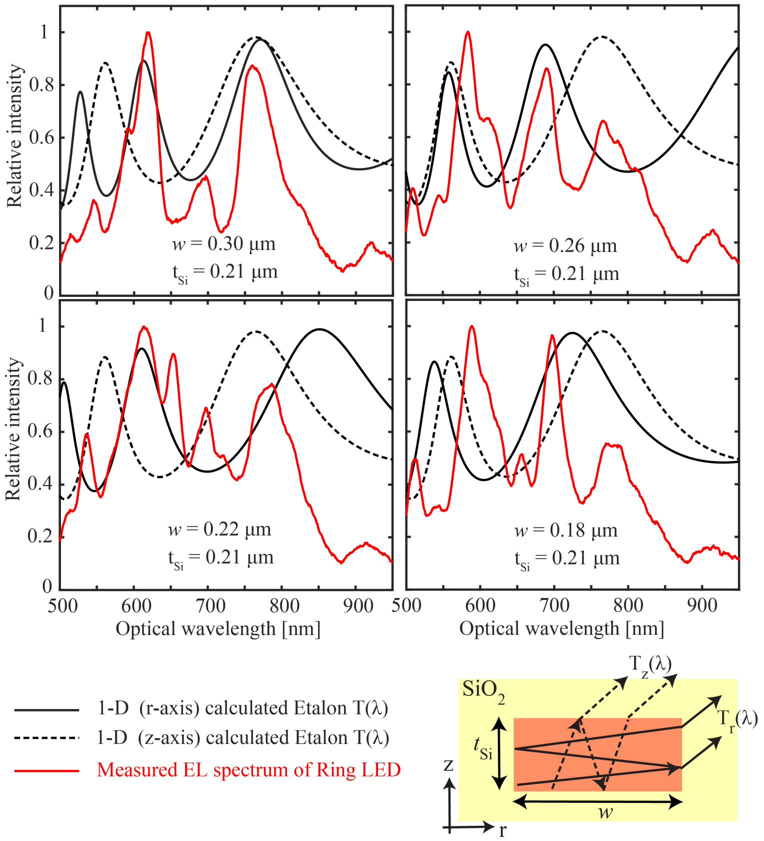

Fig. 4. Comparison between the relative AM EL intensity (red), and the calculated 1-D Fabry-Pérot resonator (etalon) transmission coefficient attributed to w (solid curves) and t_{Si} (dashed curves) for the N2-P2 doped AMLEDs with R=2.0 μm and varying w. The bottom inset shows a schematic of light rays in the optical cavity formed by the Si LED surrounded by SiO_2 in the r-z plane.

The η_{opt} in this work are an order of magnitude higher than that of prior reported Si AMLEDs (with no FP-resonance in the light-emitting Si region) as shown in Fig. 5(c), while also consuming ∼ 10 times lower electrical power per p-n junction in the LED design. The AMLEDs based on a standard BCD SOI-CMOS technology [12,32] were contained in a 1.5 μm thick SOI layer with junction depths of ~0.25 μm surrounded by SiO_2 trench isolation. AMLEDs based on the 65 nm bulk CMOS technology [50] had shallow junctions without any optical confinement of the light-emitting Si layer. The 3-terminal FET-based LEDs based in 0.18 μm bulk CMOS technology [25] employed electrostatic gate control on the η_{opt} of light emitted by shallow p^+-n junctions, with no optical confinement of the Si layer. The 3-terminal LEDs in [31] were fabricated in a 0.35 μm RF bipolar process, where the p^+-n junctions were placed in etched columns of n-type Si resting on a Si substrate.

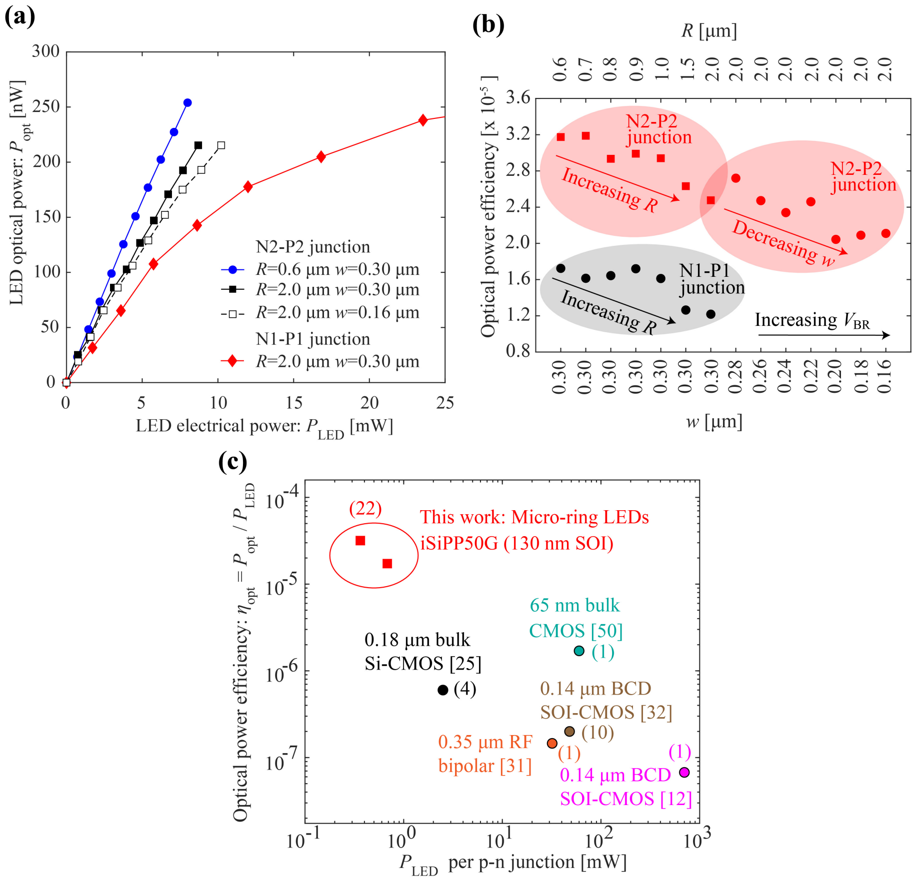

Fig. 5. (a) Measured AMLED optical power P_{opt} versus electrical power P_{LED}=$I_{LED} \cdot V_{LED}$ for the indicated design parameters. P_{opt} was measured via the photocurrent of an off-chip Si PD (as shown in Fig. 1(d)), followed by a power calibration as described in section 3 and using Eq. (1). (b) Optical power efficiency η_{opt} versus LED design parameters: doping level, R and w. (c) Benchmark of η_{opt} versus electrical power (P_{LED}) consumed per p-n junction against prior art for Si AMLEDs fabricated in the indicated technologies. The numbers within parentheses denote the number of p-n junctions present in the respective LED.

5. Discussion and outlook

Conventional Si AMLEDs emit photons with a broad range of energies exceeding the electronic bandgap, thereby exhibiting EL in both the visible and NIR spectrum. Aided by a recent CMOS-compatible silicon photonics technology [47] that allows opto-electronic integration, we have shown the effect of optical cavity resonances on hot-carrier EL in Si, an indirect bandgap semiconductor. By incorporating a p-n junction in sub-micron sized rings of varying geometry, we have shown that FP resonances–both in-plane (r-axis) and out-of-plane (z-axis)–determine $\varepsilon(\lambda)$ and results in a record-low FWHM of the peak intensity wavelengths λ_P near 600 nm and 760 nm (Figs. 3(a),(b)). The mechanism of EL at these peak wavelengths is inter-band recombination, as also observed in prior works [25,31,33,50]. FP resonance increases the exiting capability of radiation from the Si rings, and this is likely the reason for enhanced EL intensities from the ring LEDs. By varying w from 0.16 μm to 0.3 μm (Figs. 3(e),(f), and Fig. 4), we can tune λ_P across a wide spectral range (500-750 nm). Tuning the Si AMLED spectrum over such a wide range of λ constitutes a breakthrough in engineering the EL spectrum of Si, without altering its material composition. Further, we have shown that η_{opt} increases by decreasing the R / w ratio of the LEDs (Fig. 5(b)) and by choosing a high doping level that lowers the breakdown voltage to ~ 7 V. In prior works on highly-doped p-n junctions in bulk Si CMOS technology [50], and in standard BiCMOS technology [56], a maximum η_{opt} was reported–both in theory and in experiment–to occur near $V_{\text{BR}} \approx 6$ V, where V_{BR} was tuned via scaling the doped regions along the direction of current flow [50], or by changing device type (diode versus transistor) and electrical biasing [56]. A further reduction in V_{BR} led to a sharp fall in η_{opt} due to effects of non-local avalanche and carrier tunneling. Our present work, however, opens an additional route of device scaling perpendicular to the direction of current flow without altering the p-n junction profile. Future research should address if this limit can be pushed further down to 5 V (TTL logic levels) or lower by fabricating rings with even lower R/w ratio.

Our work opens new possibilities in developing an integrated Si-light source tailored for applications such as monolithic optical links and sensors. These applications are key in driving the development of co-integration of optics in CMOS-compatible technologies. Realizing λ-tunability and a high η_{opt} in Si LEDs is foreseen to boost the figures of merit in the aforesaid applications. For example, bit error rate in optical links [13,26] decreases with increasing optical energy per bit to noise ratio; the latter can be achieved at lower electrical power if η_{opt} is increased. As another example, consider an optical system to sense pigment concentration (c) [24], which comprises an LED with a $\varepsilon(\lambda)$ defined in a band $\lambda_{\text{P}} \pm \Delta\lambda$, and an ideal PD (quantum efficiency of 1) as the receiver. By applying Beer-Lambert law at low c, it can be derived that the sensitivity $S \propto \eta_{\text{opt}} \cdot \alpha_{\text{M}}^{\text{LED}}(\lambda)$, where $\alpha_{\text{M}}^{\text{LED}}(\lambda) = \int \varepsilon(\lambda) \cdot \alpha_{\text{M}}(\lambda) \cdot \mathrm{d}\lambda$ is the LED-specific molar absorption coefficient of the pigment. The $\alpha_{\text{M}}(\lambda)$ of most pigments relevant to bio-chemical sensing, e.g. chlorophyll (Chl) in plants and bacteria, feature narrow bands (FWHM ~40-80 nm) at specific values of λ_{P}. A match in λ_{P} and FWHM between $\varepsilon(\lambda)$ and $\alpha_{\text{M}}(\lambda)$ will maximize $\alpha_{\text{M}}^{\text{LED}}(\lambda)$. This will, in turn, increase S and also improve the specificity. For example, $\alpha_{\text{M}}(\lambda)$ of bacteriochlorophyll (BChl) A/B have peaks in $\lambda \sim 760$–780 nm and in $\lambda \sim 560$–590 nm [57], which overlaps well with the $\varepsilon(\lambda)$ of our ring AMLEDs with $w= 0.3$ μm and 0.22 μm. Similarly, BChl C/D and Chl A/B feature absorption peaks in $\lambda \sim 640$–660 nm, which overlaps well with the $\varepsilon(\lambda)$ of our ring AMLED with $w= 0.24$ μm.

Based on our work, optocouplers and pigment sensors can be developed using the resonant AMLEDs to benchmark the improved system performance. On a device level, the effects of further reduction in w or t_{Si}, varying the placement of the p-n junction, and varying the cavity design (e.g. disk resonators) on both η_{opt} and $\varepsilon(\lambda)$ can be investigated in future work. The motivation behind reducing w or t_{Si} is to explore the limits of wavelength tunability due to FP resonance, including a scenario where a single resonance wavelength might be observed (quasi-monochromatic LEDs). A thinner/thicker SOI layer is expected to result in a blue/red shift in the peak emission wavelength. A thinner layer could reduce the round-trip loss in the Si cavity, which is likely to further reduce the FWHM. Disk-based designs can be beneficial to further reduce the form-factor of the LEDs. Alternative placements of the p-n junction within the LED can help in tailoring the spatial light-emission profile. Lastly, a set of rings with different w (and hence, different λ_{P}) can be combined in a single AMLED to generate white light with a more uniform emission spectrum. This is foreseen to reduce pixel-size in recently reported [25] on-chip CMOS micro-display applications.

6. Conclusions

We presented a micro-ring based design of avalanche-mode (AM) silicon (Si) light-emitting diodes (LEDs), consisting of p-n junctions placed within a cavity that offers optical confinement in two dimensions. The LEDs were fabricated in a CMOS-compatible silicon-on-insulator photonics technology, with varying ring radius, width, and doping levels. Due to Fabry-Pérot resonances, the light emission spectra of the LEDs were observed to exhibit relatively narrow bands (spectral widths ~ 50 nm) with ~ 2-3 times higher intensities compared to conventional Si AMLEDs in the wavelength range from 500 nm to 950 nm. The peak wavelengths of these emission bands showed a dependence on the ring width, in accordance with the analytical model of a lossy Fabry-Pérot resonator. By scaling the ring radius to width ratio and using a high doping level, we reduced the form-factor and breakdown voltage of the LEDs. Consequently, an order-of-magnitude increase in the optical power efficiency was achieved compared to prior art. The brightest LED in our work had a radius 0.6 μm, width 0.3 μm and an optical power efficiency of 3.2×10^{-5} while consuming 360 μW of electrical power per p-n junction. Our work is a major step forward in tailoring the hot-carrier EL spectrum of silicon p-n junctions, which could boost performance and scope of all-Si optical interconnects and sensors.

Acknowledgments. This work was carried out within the Plantenna research program, supported by the Dutch 4TU Federation. The authors thank IMEC vzw, Leuven (Belgium) for device fabrication, and Europractice IC service for support with design tool and access to the multi-project wafer run. The authors also thank Rob Luttjeboer and Tufan Erdoğan for experimental support, and Wouter Westerveld for fruitful discussions.

Disclosures. The authors declare no conflicts of interest.

Data availability. Data underlying the results presented in this paper are not publicly available at this time but may be obtained from the authors upon reasonable request.

References

1. S. Y. Siew, B. Li, F. Gao, H. Y. Zheng, W. Zhang, P. Guo, S. W. Xie, A. Song, B. Dong, L. W. Luo, C. Li, X. Luo, and G.-Q. Lo, "Review of silicon photonics technology and platform development," J. Lightwave Technol. **39**(13), 4374–4389 (2021).
2. T. Claes, J. G. Molera, K. De Vos, E. Schacht, R. Baets, and P. Bienstman, "Label-Free Biosensing With a Slot-Waveguide-Based Ring Resonator in Silicon on Insulator," IEEE Photonics J. **1**(3), 197–204 (2009).
3. S. Soria, S. Berneschi, M. Brenci, F. Cosi, G. Nunzi Conti, S. Pelli, and G. C. Righini, "Optical microspherical resonators for biomedical sensing," Sensors **11**(1), 785–805 (2011).
4. X. Zheng, D. Patil, J. Lexau, F. Liu, G. Li, H. Thacker, Y. Luo, I. Shubin, J. Li, J. Yao, P. Dong, D. Feng, M. Asghari, T. Pinguet, A. Mekis, P. Amberg, M. Dayringer, J. Gainsley, H. F. Moghadam, E. Alon, K. Raj, R. Ho, J. E. Cunningham, and A. V. Krishnamoorthy, "Ultra-efficient 10 Gb/s hybrid integrated silicon photonic transmitter and receiver," Opt. Express **19**(6), 5172–5186 (2011).
5. C. Sun, M. T. Wade, and Y. Lee, *et al.*, "Single-chip microprocessor that communicates directly using light," Nature **528**(7583), 534–538 (2015).
6. M. J. Lee, P. Sun, and E. Charbon, "A first single-photon avalanche diode fabricated in standard SOI CMOS technology with a full characterization of the device," Opt. Express **23**(10), 13200–13209 (2015).
7. M. A. Green, J. Zhao, A. Wang, P. J. Reece, and M. Gal, "Efficient silicon light-emitting diodes," Nature **412**(6849), 805–808 (2001).
8. L. W. Snyman, M. du Plessis, and H. Aharoni, "Injection-avalanche-based n^+-p-n silicon complementary metal-oxide-semiconductor light-emitting device (450–750 nm) with 2-order-of-magnitude increase in light emission intensity," Jpn. J. Appl. Phys. **46**(4B), 2474–2480 (2007).
9. C. Schinke, D. Hinken, J. Schmidt, K. Bothe, and R. Brendel, "Modeling the spectral luminescence emission of silicon solar cells and wafers," IEEE J. Photovoltaics **3**(3), 1038–1052 (2013).
10. B. Huang, X. Zhang, W. Wang, Z. Dong, N. Guan, Z. Zhang, and H. Chen, "CMOS monolithic optoelectronic integrated circuit for on-chip optical interconnection," Opt. Commun. **284**(16-17), 3924–3927 (2011).
11. A. Khanmohammadi, R. Enne, M. Hofbauer, and H. Zimmermann, "Monolithic integrated optical random pulse generator in high voltage CMOS technology," in *Proc. European Solid-State Device Research Conference (ESSDERC)*2015, pp. 138–141.
12. S. Dutta, V. Agarwal, R. J. E. Hueting, J. Schmitz, and A.-J. Annema, "Monolithic optical link in silicon-on-insulator CMOS technology," Opt. Express **25**(5), 5440–5456 (2017).
13. V. Agarwal, S. Dutta, A.-J. Annema, R. J. E. Hueting, J. Schmitz, M.-J. Lee, E. Charbon, and B. nauta, "Optocoupling in CMOS," in *Proc. International Electron Devices Meeting (IEDM)*, Technical Digest, pp. 739–742 (2018).
14. C. Roques-Carmes, S. E. Kooi, Y. Yang, A. Massuda, P. D. Keathley, A. Zaidi, Y. Yang, J. D. Joannopoulos, K. K. berggren, I. Kaminer, and M. Soljačić, "Towards integrated tunable all-silicon free-electron light sources," Nat. Commun. **10**(1), 3176 (2019).
15. S. W. Schmitt, K. Schwarzburg, G. Sarau, S. H. Christiansen, S. Wiesner, and C. Dubourdieu, "All-silicon polarized light source based on electrically excited whispering gallery modes in inversely tapered photonic resonators," APL Mater. **8**(6), 061110 (2020).
16. R. Newman, "Visible light from a silicon p-n junction," Phys. Rev. **100**(2), 700–703 (1955).

17. A. G. Chynoweth and K. G. McKay, "Photon emission from avalanche breakdown in silicon," Phys. Rev. **102**(2), 369–376 (1956).
18. M. D. Plessis, H. Aharoni, and L. W. Snyman, "Silicon LEDs fabricated in standard VLSI technology as components for all silicon monolithic integrated optoelectronic systems," IEEE J. Sel. Top. Quantum Electron. **8**(6), 1412–1419 (2002).
19. B. P. van Drieënhuizen and R. F. Wolffenbuttel, "Optocoupler based on the avalanche light emission in silicon," Sens. Actuators, A **31**(1-3), 229–240 (1992).
20. M. Ramamurthy and V. Lakshminarayanan, "Human vision and perception," in R. Karlicek, C. C. Sun, G. Zissis, and R. Ma (eds.), *Handbook of Advanced Lighting Technology* (Springer, 2015).
21. H. Croft and J. M. Chen, "Leaf pigment content," in S. Lian (ed.), *Comprehensive Remote Sensing*, vol. 3, (Elsevier, Amsterdam, The Netherlands, 2018) Chap. 8, pp. 117–142.
22. L. Li, A. A. Shemetov, M. Baloban, P. Hu, L. Zhu, D. M. Shcherbakova, R. Zhang, J. Shi, J. Yao, L. V. Wang, and V. V. Verkhusha, "Small near-infrared photochromic protein for photoacoustic multi-contrast imaging and detection of protein interactions in vivo," Nat. Commun. **9**(1), 2734 (2018).
23. S. K. Lazarouk, A. A. Leshok, T. A. Kozlova, A. V. Dolblik, L. D. Vi, V. K. Ilkov, and V. A. Labunov, "3D silicon photonic structures based on avalanche LED with interconnections through optical interposer," Int. J. Nanosci. **18**(03n04), 1–5 (2019).
24. S. Dutta, P. G. Steeneken, and G. J. Verbiest, "Optical sensing of chlorophyll(in) with dual-spectrum Si LEDs in SOI-CMOS technology," IEEE Sensors J. **22**(12), 11280–11289 (2022).
25. K. Wu, H. Zhang, Y. Chen, Q. Luo, and K. Xu, "All-Silicon microdisplay using efficient hot-carrier electroluminescence in standard 0.18 μm CMOS technology," IEEE Electron Device Lett. **42**(4), 541–544 (2021).
26. V. Agarwal, S. Dutta, A.-J. Annema, R. J. E. Hueting, P. G. Steeneken, and B. Nauta, "Low power wide spectrum optical transmitter using avalanche mode LEDs in SOI CMOS technology," Opt. Express **25**(15), 16981–16995 (2017).
27. M. O'Toole, K. T. Lau, R. Shepherd, C. Slater, and D. Diamond, "Determination of phosphate using a highly sensitive paired emitter-detector diode photometric flow detector," Anal. Chim. Acta **597**(2), 290–294 (2007).
28. M. O'Toole and D. Diamond, "Absorbance based light emitting diode optical sensors and sensing devices," Sensors **8**(4), 2453–2479 (2008).
29. P. Yeh, N. Yeh, C.-H. Lee, and T.-J. Ding, "Applications of LEDs in optical sensors and chemical sensing device for detection of biochemicals, heavy metals, and environmental nutrients," Renewable Sustainable Energy Rev. **75**, 461–468 (2017).
30. L. W. Snyman, K. Xu, J.-L. Polleux, K. A. Ogudo, and C. Viana, "Higher intensity SiAvLEDs in an RF bipolar process through carrier energy and carrier momentum engineering," IEEE J. Quantum Electron. **51**(7), 1–10 (2015).
31. L. W. Snyman, K. Xu, and J.-L. Polleux, "Micron and nano-dimensioned silicon LEDs emitting at 650 and 750-850 nm wavelengths in standard Si integrated circuitry," IEEE J. Quantum Electron. **56**(4), 1–10 (2020).
32. S. Dutta, P. G. Steeneken, V. Agarwal, J. Schmitz, A.-J. Annema, and R. J. E. Hueting, "The avalanche-mode superjunction LED," IEEE Trans. Electron Devices **64**(4), 1612–1618 (2017).
33. K. Xu and G. P. Li, "A three terminal silicon PMOSFET light emitting device (LED) for optical intensity modulation," IEEE Photonics J. **4**(6), 2159–2168 (2012).
34. K. Xu, "Silicon electro-optic micro-modulator fabricated in standard CMOS technology as components for all silicon monolithic integrated optoelectronic systems," J. Micromech. Microeng. **31**(5), 054001 (2021).
35. E. F. Schubert, Y.-H. Wang, A. Y. Cho, L.-W. Tu, and G. J. Zydzik, "Resonant cavity light-emitting diode," Appl. Phys. Lett. **60**(8), 921–923 (1992).
36. C. K. Tseng, H. W. Hung, J. R. Huang, K. Y. Lee, G. R. Lin, J. M. Shieh, and M. C. M. Lee, "Silicon-nanocrystal resonant-cavity light-emitting devices for color tailoring," in *Proc. International Quantum Electronics Conference (IQEC) and Conference on Lasers and Electro-Optics (CLEO) Pacific Rim*, 2011, pp. 1009–1011.
37. E. Dahal, D. Allemeier, B. Isenhart, K. Cianciulli, and M. S. White, "Characterization of higher harmonic modes in Fabry–Pérot microcavity organic light emitting diodes," Sci. Rep. **11**(1), 8456 (2021).
38. C. A. Barrios and M. Lipson, "Electrically driven silicon resonant light emitting device based on slot-waveguide," Opt. Express **13**(25), 10092–10101 (2005).
39. M. Bugajski, J. Muszalski, B. Mroziewicz, K. Reginski, and T. J. Ochalski, "Resonant cavity enhanced photonic devices," Opt. Appl. **XXXI**(2), 273–288 (2001).
40. R. G. Baets, D. Delbeke, R. Bockstaele, and P. Bienstman, "Resonant cavity light-emitting diodes: a review," Proc. SPIE **4996**, 74–86 (2003).
41. M. Casalino, G. Coppola, M. Iodice, I. Rendina, and L. Sirleto, "Critically coupled silicon Fabry-Perot photodetectors based on the internal photoemission effect at 1550 nm," Opt. Express **20**(11), 12599–12609 (2012).
42. M. Casalino, "Theoretical Investigation of Near-Infrared Fabry–Pérot Microcavity Graphene/Silicon Schottky Photodetectors Based on Double Silicon on Insulator Substrates," Micromachines **11**(8), 708 (2020).
43. X. Chen, X. Yang, Q. Lou, Y. Zhang, Y. Chen, Y. Lu, L. Dong, and C.-X. Shan, "Fabry-Perot interference and piezo-phototronic effect enhanced flexible MoS_2 photodetector," Nano Res. **15**(5), 4395–4402 (2022).
44. K.-H. Lin, C.-M. Lai, C.-C. Pan, J.-I. Chyi, J.-W. Shi, S.-Z. Sun, C.-F. Chang, and C.-K. Sun, "Spatial manipulation of nanoacoustic waves with nanoscale spot sizes," Nat. Nanotechnol. **2**(11), 704–708 (2007).

45. D. Ochoa, R. Houdré, M. Ilegems, C. Hanke, and B. Borchert, "Microcavity light emitting diodes as efficient planar light emitters for telecommunication applications," C.R. Physique **3**(1), 3–14 (2002).
46. K. F. Renk, "Fabry Perot resonator," in *Basics of Laser Physics* (Springer-Verlag, 2012), Chap. 3, pp. 43–54.
47. P. P. Absil, P. De Heyn, H. Chen, P. Verheyen, G. Lepage, M. Pantouvaki, J. De Coster, A. Khanna, Y. Drissi, D. Van Thourhout, and J. Van Campenhout, "Imec iSiPP25G silicon photonics: a robust CMOS-based photonics technology platform," Proc. SPIE **9367**, 93670V (2015).
48. S. M. Sze and K. K. Ng, *Physics of semiconductor devices* (3rd ed. Wiley, 2012).
49. S. Dutta, R. J. E. Hueting, A.-J. Annema, L. Qi, L. K. Nanver, and J. Schmitz, "Opto-electronic modeling of light emission from avalanche-mode silicon p^+n junctions," J. Appl. Phys. **118**(11), 114506 (2012).
50. S. Dutta, G. J. M. Wienk, R. J. E. Hueting, J. Schmitz, and A.-J. Annema, "Optical power efficiency versus breakdown voltage of avalanche-mode silicon LEDs in CMOS," IEEE Electron Device Lett. **38**(7), 898–901 (2017).
51. M. A. Green, "Self-consistent optical parameters of intrinsic silicon at 300K including temperature coefficients," Sol. Energy Mater. Sol. Cells **92**(11), 1305–1310 (2008).
52. M. Hammer, "1-D mode solver for dielectric multilayer slab waveguides," Software on line available at: https://www.siio.eu/oms.html (2022).
53. M. Hammer, "1-D mode solver for 1-D mode solver for slab waveguide bends," Software on line available at: https://www.computational-photonics.eu/bends.html (2022).
54. P. Wessels, M. Swanenberg, H. van Zwol, B. Krabbenberg, H. Boezen, M. Berkhout, and A. Grakist, "Advanced BCD technology for automotive, audio and power applications," Solid-State Electron. **51**(2), 195–211 (2007).
55. E. F. Schubert, *Light Emitting Diodes* (Cambridge University Press, 2006).
56. P. I. Kuindersma, T. Hoang, J. Schmitz, M. N. Vijayaraghavan, M. Dijkstra, W. van Noort, T. Vanhoucke, W. C. M. Peters, and M. C. J. C. M. Kramer, "The power conversion efficiency of visible light emitting devices in standard BiCMOS processes," in *proc. 5th IEEE International Conference on Group IV Photonics* (2008), pp. 256–258.
57. A. Oren, "Characterization of pigments of prokaryotes and their use in taxonomy and classification," Methods Microbiol. **38**(11), 261–282 (2011).